Check for updates

18673899, 2021, 18, Downloaded from https://chemistry-europe.onlinelibrary.wiley.com/doi/10.1002/cctc.202100858 by Cochrane Germany, Wiley Online Library on [28/11/2022]. See the Terms and Conditions (https://onlinelibrary.wiley.com/terms-and-conditions) on Wiley Online Library for rules of use; OA articles are governed by the applicable Creative Commons License

Mixed $Ru_xIr_{1-x}O_2$ Supported on Rutile TiO_2: Catalytic Methane Combustion, a Model Study

Omeir Khalid,[a, b] Alexander Spriewald Luciano,[a, b] Goran Drazic,[c] and Herbert Over*[a, b]

With a modified Pechini synthesis, mixed $Ru_xIr_{1-x}O_2$ is grown on rutile-TiO_2 with full control of the composition x, where the preformed TiO_2 particles serve as nucleation sites for the active component. Catalytic and kinetic data of the methane combustion over $Ru_xIr_{1-x}O_2$@TiO_2 and unsupported $Ru_xIr_{1-x}O_2$ catalysts reveal that the least active catalyst is RuO_2@TiO_2 (onset temperature: 270 °C), while the most active catalyst is $Ru_{0.25}Ir_{0.75}O_2$ with an onset temperature below 220 °C. Surprisingly, even $Ru_{0.75}Ir_{0.25}O_2$@TiO_2 is remarkably active in methane combustion (onset temperature: 230 °C), indicating that little iridium in the mixed $Ru_xIr_{1-x}O_2$ oxide component already improves the activity of the methane combustion considerably. We conclude that iridium in the mixed $Ru_xIr_{1-x}O_2$ oxide enables efficient methane activation, while ruthenium promotes the subsequent oxidation steps of the methyl group to produce CO_2. Kinetic data provide a reaction order in O_2 of zero, while that of methane is close to one, indicating that the methane activation is rate limiting. The apparent activation energy varies among $Ru_xIr_{1-x}O_2$ from 110 ($x=0$) to 80 kJ·mol^{-1} ($x=1$). This variation in the apparent activation energy may be explained by the variation in adsorption energy of oxygen. Under the given reaction conditions the catalyst's surface is saturated with adsorbed oxygen and only if oxygen desorbs, methane can be activated and the methyl group can be accommodated at the liberated surface metal sites.

1. Introduction

Methane, the primary constituent of natural gas, is a promising alternative fuel in mobile and stationary applications due to its relatively high abundance, lower cost compared to other fuels and the lowest C/H ratio among organic molecules so that combustion leads to the lowest amount of CO_2 per energy unit.[1,2] Methane is also a promising energy vector for future circular energy economy based on renewable energies.[3]

However, methane is a potent greenhouse gas with a global warming factor that is 28–34 times higher than that of CO_2. Therefore, the use of natural- and biogas based fuels in transportation requires an efficient oxidation catalyst in particular under lean conditions to prevent methane-slip to the atmosphere.[4] Unfortunately, methane is the most difficult hydrocarbon to catalytically oxidize so that a relatively high temperature is needed for the reaction to proceed with an acceptable rate.[5,6]

While several studies about non noble-metal catalysts such as perovskite type materials with high activity have been reported over the last two decades,[7,8,9] palladium based catalysts are generally considered to be the most promising candidates for methane combustion.[1,10–13] Especially at low reaction temperatures Pd is more active than rhodium and platinum.[3,10,12] There is general consensus that higher temperatures stabilize the metallic Pd as the (more) active phase, while at lower temperatures PdO governs the stable activity.[14] Pd or rather PdO has shown even higher activities when supported on γ-Al_2O_3, demonstrating beneficial interactions between the support and the active component.[15] Since Pt and Rh show also high activity in methane combustion (although less active than Pd),[3] the methane combustion activity may be traced to properties typical for the platinum group members to which ruthenium and iridium belong.

Recently, an oxidized Ir(100) single-crystalline surface was reported to be surprisingly efficient in the low-temperature methane activation. In temperature programmed reaction (TPR) experiments the oxidized surface of Ir(100) was covered with methane (and oxygen) at temperatures below −173 °C and then the products were recorded with mass spectrometry while ramping the sample to 427–527 °C.[16,17] The active phase has been assigned to a IrO_2(110) layer, as previously predicted by Wang et al. on the basis of density functional theory (DFT) calculations.[18] We should emphasize here that these TPR experiments are mere transient and not catalytic experiments; for catalytic experiments one needs to demonstrate steady state conversion under flow reaction conditions. The methane

[a] O. Khalid, A. Spriewald Luciano, Prof. H. Over
Physikalisch-Chemisches Institut
Justus Liebig University
Heinrich-Buff-Ring 17
35392 Giessen (Germany)
E-mail: Herbert.Over@phys.Chemie.uni-giessen.de
[b] O. Khalid, A. Spriewald Luciano, Prof. H. Over
Zentrum für Materialforschung
Justus Liebig University
Heinrich-Buff-Ring 16
35392 Giessen (Germany)
[c] G. Drazic
Department of Materials Chemistry
National Institute of Chemistry
Hajdrihova 19
1000 Ljubljana (Slovenia)

Supporting information for this article is available on the WWW under https://doi.org/10.1002/cctc.202100858

© 2021 The Authors. ChemCatChem published by Wiley-VCH GmbH. This is an open access article under the terms of the Creative Commons Attribution License, which permits use, distribution and reproduction in any medium, provided the original work is properly cited.

activation process was further examined by in-situ DRIFTS and Raman experiments for IrO_2 nanoparticles in a constant flow of pure CH_4, emphasizing the important role of the oxidation state of iridium.[19] Metallic iridium (supported on alumina) has briefly explored as a part of catalyst screening of noble metals for methane combustion at 475 °C, revealing, however, iridium to be inferior to the remaining platinum group members.[20]

While IrO_2 is efficient for methane activation,[16] its total oxidation capability is quite poor as demonstrated by a recent study on the CO oxidation over $Ru_xIr_{1-x}O_2$ powder catalysts with the composition x ranging from 0 to 100 mol%.[21] Quite in contrast, RuO_2 is well-documented to be an efficient oxidation catalyst.[22] Therefore, we anticipated that mixed $Ru_xIr_{1-x}O_2$ may offer synergy effects for the combustion of methane by promoting the methane activation step by iridium, while the subsequent oxidation steps towards CO_2 are promoted by ruthenium centers.

In order to have full control of the composition of the mixed $Ru_xIr_{1-x}O_2$ oxide component we designed a modified Pechini synthesis route where preformed rutile-TiO_2 powder was used to provide nucleation sites for the formation and deposition of $Ru_xIr_{1-x}O_2$, thereby producing a supported $Ru_xIr_{1-x}O_2$@TiO_2 catalyst with well-defined composition x. In this study we present catalytic and kinetic data for the methane combustion over supported $Ru_xIr_{1-x}O_2$@rutile TiO_2 catalysts in comparison with data from unsupported powder $Ru_xIr_{1-x}O_2$. This paper focuses on the intrinsic activity in the combustion of methane, and how this activity can be modified by mixing RuO_2 with IrO_2.

Experimental Details

Modified Pechini synthesis

The synthesis of unsupported $Ru_xIr_{1-x}O_2$ was described recently.[21] The supported catalysts ($Ru_xIr_{1-x}O_2$@TiO_2) were synthesized with a modification of the Pechini route[23] by adding pure rutile-TiO_2 (particle size $<$ 100 nm) before complexation of the ruthenium- and iridium-cations by citric acid. Rutile TiO_2 as carrier was chosen since we expected a high dispersion of rutile $Ru_xIr_{1-x}O_2$ from previous surface science studies of RuO_2 and IrO_2 on rutile TiO_2(110).[24,25] The added rutile-TiO_2 support particles are trapped in the carbon network after polymerization of citric acid and ethylene glycol. The ruthenium and iridium cations either nucleate directly on the support surface or mixed ruthenium-iridium particles nucleate first and then adhere to the support material, resulting in both cases in highly dispersed supported ruthenium-iridium mixed oxide particles after final calcination.

Throughout the manuscript the supported samples are referred to as Ru_x@TiO_2, with x being the nominal composition of ruthenium in mol% changing from 0 mol% to 100 mol% in steps of 25 mol% (pure iridium sample is referred to as Ir_100@TiO_2 instead of Ru_0@TiO_2) while unsupported powder catalysts are abbreviated by Ru_x. The relative amount of active component with respect to the support is chosen to be 5 mol%. This amount represents a reasonable compromise for having enough active component for in-depth characterization and catalytic measurements, while being low enough to ensure that most of the active component is supported on rutile TiO_2. Further details on the preparation of supported materials can be found in the supporting information.

Characterization techniques

The samples were degassed in vacuum for 12 h at 120 °C before conducting Kr-physisorption experiments at −196 °C with the Autosorb 6 of Quantachrome. The Brunauer-Emmett-Teller (BET) method was employed to quantify the specific surface area (referred to as *BET*), regardless of whether this comes from the active component or from the carrier.

The CO-pulse-experiments (CO up-take experiments) were conducted in a home-built apparatus in order to determine the *number of active sites* provided by the active component of the ruthenium-iridium mixed oxide samples. In general, the titration experiment quantifies the amount of accessible surface noble-metal atoms per gram catalyst according to the number of adsorbed CO molecules.[26–28] With the approximation that each of these ruthenium/iridium sites is an active center for the methane conversion the *number of active sites* is equal to the number of adsorbed CO molecules. Even if this approximation of every metal site being an active center might not entirely be correct, it still provides the relative concentration of the *number of actives sites* between the different samples for a proper normalization of the catalytic *STY* (*space time yield*) data to the accessible surface of the supported active component.

X-ray diffraction (XRD) measurements were carried out in Θ–2Θ geometry (Bragg Brentano) on a Panalytical X'Pert PRO diffractometer with a Cu Kα source (40 kV, 40 mA) with a step size of 0.013° in 2Θ and a scanning speed of about 0.8° min^{-1}. LaB_6 standards (NIST) were added to correct the 2Θ shift due for instance to different sample holder positions. The position of the rutile ruthenium-iridium mixed oxide (101) reflection can be used to determine the composition of that oxide by Vegard's law.[21]

The ratio of iridium to ruthenium concentration in the near-surface region of the Ru_x@TiO_2 samples was quantified by X-ray photoelectron spectroscopy (XPS) (PHI VersaProbe II). Deconvolution of the XP spectra are performed using the CASAXPS software.

Low resolution transmission electron microscopy (TEM) was performed on a Philipps CM30 instrument operated at 300 kV. For detailed structural, morphological and chemical analysis, a Cs probe-corrected scanning transmission electron microscope (STEM) was employed. Further details about the used characterization techniques are collected in the supporting information.

Flow reactor for methane combustion reaction

The catalytic and kinetic experiments are conducted in a home-built reactor system (cf. Figure S1). With mass flow controllers (MFC, MKS Instruments 1179 C) the desired reaction feed is mixed, consisting of CH_4 and O_2 balanced by N_2, and fed into the reactor that consists of a quartz tube, 6 mm inner diameter, placed in a *ThermConcept* tube furnace. The catalytic experiments are designed to collect microkinetically controlled activity data so that the reactor is employed in a differential way (further description is given in the supporting information). The purities of used gases CH_4 (Linde) and O_2 (NipponGases) are 4.7 and 4.0, respectively. The carrier gas nitrogen is generated by the Hampson-Linde cycle so that it must be dried and purified prior to admission to the mass flow system. A nondispersive infrared (NDIR)-sensor detects the volumetric concentration of C–H bonds giving the portion of CH_4. CO_2 is also detected and used primarily to quantify the space time yield [Eq. (1)]

$$STY \sim Vol\%(CO_2) \cdot \dot{V}_{total} \cdot m_{cat}{}^{-1} \quad (1)$$

© 2021 The Authors. ChemCatChem published by Wiley-VCH GmbH

18673899, 2021, 18, Downloaded from https://chemistry-europe.onlinelibrary.wiley.com/doi/10.1002/cctc.202100858 by Cochrane Germany, Wiley Online Library on [28/11/2022]. See the Terms and Conditions (https://onlinelibrary.wiley.com/terms-and-conditions) on Wiley Online Library for rules of use; OA articles are governed by the applicable Creative Commons License

where $\dot{V}_{total}$ is the total volume flow rate. In this work the catalytic performance is quantified by the space time yield *STY* ([mol $(CO_2)\cdot h^{-1}\cdot kg_{cat}^{-1}$]) which is easily calculated by the detectable variables. Under the chosen reaction conditions, we do not detect any trace of CO (NDIR) and H_2 (GCMS) in the product stream. For a direct comparison among the studied samples the *STY* can also be normalized to the *number of actives sites* (CO-pulse-experiments) that is proportional to the turnover frequency (*TOF*). A mass flow meter downstream the reactor measures the apparent total flow rate $\dot{V}_{total,apparent}$ which can be converted to the actual $\dot{V}_{total}$, besides the CO_2 concentration, required to quantify the *space time yield* [Eq. (4)]. Further details are provided in the supporting information. With a height of the catalyst bed of about 1.5 mm and a diameter of 6 mm the gas hourly space velocity is about $1.64\cdot10^5\ h^{-1}$ [Eq. (2)]

$$v_{GHSV} = \frac{\dot{V}_{total}}{V_{catalyst\ bed}} = \frac{115cm^3\cdot min^{-1}}{0.042cm^3} \quad (2)$$

or 345.000 $ml\cdot g^{-1}\cdot h^{-1}$ if normalized to the average *mass of catalyst* [Eq. (3)].

$$v_{GHSV}^{*} = \frac{\dot{V}_{total}}{m_{cat}} = \frac{115cm^3\cdot min^{-1}}{0.02\ g} \quad (3)$$

The catalyst bed has been prepared by placing the pure sample (10 mg to 30 mg) on a 1 mm thick layer of quartz sand in order to obtain a catalyst bed as flat as possible that is important for accurate kinetic data. Analogous the catalyst material is covered with a 1 mm thick layer of quartz to prevent the nano-powder from carrying away downstream. The entire reactor is placed vertically in the oven to maintain a stable shape of catalyst bed during operation.

2. Experimental Results

2.1. Characterization of mixed ruthenium-iridium supported on rutile-TiO_2

With XPS we investigated the actual near-surface composition of the supported ruthenium-iridium catalysts (Ru_*x*@TiO_2) for varying nominal composition *x* (cf. Figure 1); in these spectra the background and the C1s component are subtracted for clarity reasons. From the energetic positions of the main components in the Ru3d spectra (cf. Figure 1a) we can clearly conclude that ruthenium is always in the 4+ oxidation state with no sign of metallic Ru (cf. Figure 1c). The Ir4f spectra are dominated by Ir^{4+} (cf. Figure 1b) but exhibit also some minor contribution of metallic Ir (cf. Figure 1c). Similar results were reported for the unsupported mixed ruthenium-iridium oxide samples[21] and were interpreted in terms of agglomerates of oxide particles adhering to a buried mixed metal particle. Therefore, the observed methane combustion activity can solely be ascribed to the mixed oxide phase. In Figure 1c detailed deconvolutions of experimental Ru3d and Ir4f XP spectra are shown exemplarily for the Ru_25@TiO_2 sample; the deconvolution of the other samples can be found in the supporting information (cf. Figure S2, Table S1).

Within the XP spectra of a single sample, the intensities of Ru3d and Ir4f are strictly correlated so that from these spectra the mean ruthenium and iridium composition as well as the composition *x* of the mixed oxide component $Ru_xIr_{1-x}O_2$@TiO_2

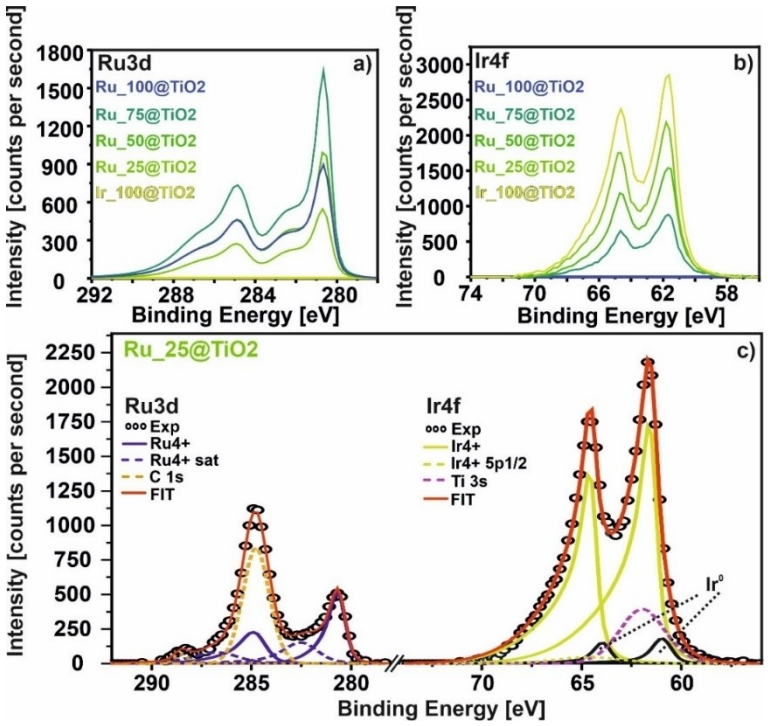


Figure 1. XP spectra of Ru_*x*@TiO_2 samples in the spectral region of Ru3d (a) and Ir4f (b). The Ru3d the spectra shown are derived by subtracting the background as well as the C1s signal derived by deconvolution using the CASAXPS software. The Ir4f spectra have been derived by subtracting the background. c) Deconvolution of the Ru3d and Ir4f spectra exemplified with the Ru_25@TiO_2 sample. Note that both spectra have identical intensity axis, thus emphasizing the relative intensity of Ru3d and Ir4f.

© 2021 The Authors. ChemCatChem published by Wiley-VCH GmbH

18673899, 2021, 18, Downloaded from https://chemistry-europe.onlinelibrary.wiley.com/doi/10.1002/cctc.202100858 by Cochrane Germany, Wiley Online Library on [28/11/2022]. See the Terms and Conditions (https://onlinelibrary.wiley.com/terms-and-conditions) on Wiley Online Library for rules of use; OA articles are governed by the applicable Creative Commons License

of each sample can be determined quite accurately; recall that the active components form solid solutions as for the unsupported system.[21,29] For determining the mean composition, the integral intensity of Ru3d and Ir4f (without C1s in case of Ru3d and background) are used, while for determining the composition *x* of the mixed oxide, only the integral intensity of Ru^{4+}3d and Ir^{4+}4f are taken. The thus estimated compositions remarkably agree with the nominal composition as given by the molar ratio of the used precursors in the synthesis (see. Table 1), emphasizing the high level of control of the composition of the supported mixed oxides.

However, the intensities among the Ru3d and Ir4f of different samples are not strictly correlated due to slightly varying experimental conditions and to varying dispersion of the active component supported on the rutile-TiO_2. Yet, a comparison of the experimental Ru3d and Ir4f spectra in Figure 1a,b reveals that the intensity variation among the Ru3d (Ir4f) spectra qualitatively reflects the concentration of the nominal ruthenium (iridium) of all samples, but the pure Ru_100@TiO_2, whose intensity is close to that of Ru_50@TiO_2.

Table 1. XPS analysis: Mean composition (independent of oxidation state) of the Ru_x@TiO_2 samples, composition of the oxide component ($Ru_xIr_{1-x}O_2$@TiO_2), and the overall noble metal (ruthenium + iridium) content given in mol% with respect to the support material TiO_2. Further details of the quantification are given in the supporting information (cf. Table S2).

Nominal	Mean composition (independent of oxidation state)			Mixed rutile oxide composition	
x (Ru_x@TiO_2) [mol%]	Ir/(Ir + Ru) [mol%]	Ru/(Ir + Ru) [mol%]	(Ru + Ir)/(Ru + Ir + Ti) [mol%]	Ir^{4+}/(Ir^{4+} + Ru^{4+}) [mol%]	Ru^{4+}/(Ir^{4+} + Ru^{4+}) [mol%]
0	100	0	24	100	0
25	78	22	23	76	24
50	56	44	17	54	46
75	28	72	19	24	76
100	0	100	14	0	100

The experimental spectra can, however, be normalized to the integral Ti2p intensity and additionally to the actual concentration of iridium and ruthenium as given in Table S2 (cf. Figure S3). From these normalized spectra one can determine the relative near-surface amount of the active component (Ru + Ir)/(Ru + Ir + Ti) that nominally should be 5 mol%. We can clearly see in Table 1 that these values are several times higher than 5 mol%, thus indicating substantial dispersion of the active component. Also obvious is that the dispersion of pure Ru_100@TiO_2 is the lowest among the mixed samples Ru_*x*@TiO_2. Further details are provided in the supporting information (cf. Tables S3, S4).

With powder XRD we examine the structure of the supported catalysts (cf. Figure 2a). The XRD scans are governed by the rutile-TiO_2 support, but there is also a faint but clearly visible (101) reflection of mixed ruthenium-iridium oxide that shifts with increasing ruthenium concentration to higher diffraction angles. In order to be able to quantify this shift, we employed LaB_6 with its sharp reflections to calibrate the 2-theta axis. This allows us to determine the chemical composition of the mixed ruthenium-iridium oxide utilizing a Vegard plot (cf. Figure 2b).[21,30]

These composition values together with the full width half maximum (*FWHM*) of the (101) reflection of the mixed oxide and the mean crystallite sizes derived from the Scherrer equation are collected in Table 2. Actually, for mixed oxides, one needs to apply the William-Hall analysis instead of the Scherrer equation to extract the mean *crystallite size*. However, the William-Hall analysis requires several mixed oxide reflections in XRD to disentangle the *crystallite size* from microstrain. Since, there is only one $Ru_xIr_{1-x}O_2$ related reflection in our experimental XRD data the Scherrer equation is used as a first estimation for the crystallite size.

The *FWHM* decreases considerably with the chemical composition *x* ($Ru_xIr_{1-x}O_2$@TiO_2), that is associated with an increase of the crystallite size of the mixed ruthenium-iridium oxide particles. For Ir_100@TiO_2 the *crystallite size* is the smallest with 7 nm, while with increasing ruthenium concentration the

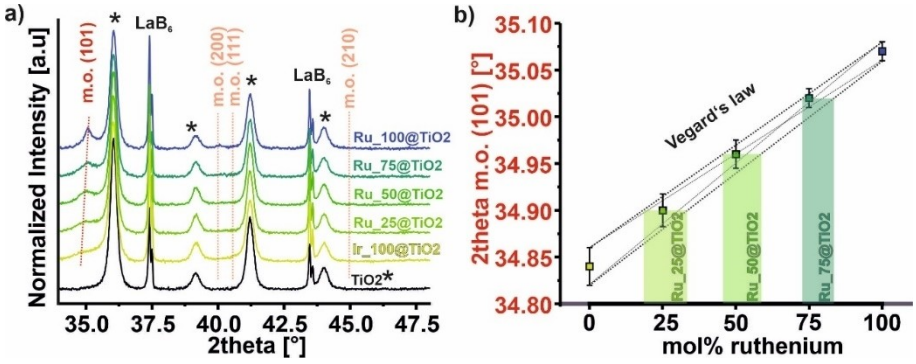


Figure 2. XRD patterns of supported Ru_*x*@TiO_2 samples normalized to TiO_2(101) reflection. LaB_6 was added for calibrating the 2theta axis. The (101) reflection of ruthenium-iridium mixed oxide is indicated. Growth and sharpening of the (101) reflection with higher amount of ruthenium evidence that the particle size increases with higher ruthenium content. All reflections which are marked with * belong to the pure support material rutile TiO_2. The (101) diffraction line is the only clearly visible one for the mixed $Ru_xIr_{1-x}O_2$ oxide (m. o.) component in the shown 2 theta range. The (200) at about 40.0°, the (111) at about 40.5° and the (210) at about 45.0° of the mixed $Ru_xIr_{1-x}O_2$ oxide are buried in the background noise since all these diffraction lines have one to three orders of magnitude lower intensities.

© 2021 The Authors. ChemCatChem published by Wiley-VCH GmbH

18673899, 2021, 18, Downloaded from https://chemistry-europe.onlinelibrary.wiley.com/doi/10.1002/cctc.202100858 by Cochrane Germany, Wiley Online Library on [28/11/2022]. See the Terms and Conditions (https://onlinelibrary.wiley.com/terms-and-conditions) on Wiley Online Library for rules of use; OA articles are governed by the applicable Creative Commons License

18673899, 2021, 18, Downloaded from https://chemistry-europe.onlinelibrary.wiley.com/doi/10.1002/cctc.202100858 by Cochrane Germany, Wiley Online Library on [28/11/2022]. See the Terms and Conditions (https://onlinelibrary.wiley.com/terms-and-conditions) on Wiley Online Library for rules of use; OA articles are governed by the applicable Creative Commons License

Table 2. XRD analysis: Composition of the oxide component ($Ru_xIr_{1-x}O_2@TiO_2$) of the supported mixed ruthenium-iridium materials derived by Vegard's law as well as the full width half maximum (FWHM) indicating bigger crystallites with higher content of ruthenium. The XRD results are compared to the average particle size as obtained from TEM.

	Ir_100@TiO_2	Ru_25@TiO_2	Ru_50@TiO_2	Ru_75@TiO_2	Ru_100@TiO_2
x ($Ru_xIr_{1-x}O_2@TiO_2$)	0	0.28 ± 0.07	0.53 ± 0.06	0.79 ± 0.05	1
FWHM [°2Theta]	1.2	1.1	0.9	0.8	0.4
XRD: Crystallite size [nm]	7	8	10	11	22
TEM: Particle size [nm]	4	5	6	6	11

mean *crystallite size* steadily increases to 11 nm for Ru_75@TiO_2. This size effect is most prominent with the pure RuO_2@TiO_2 system (referred to as Ru_100@TiO_2) with a mean *crystallite size* of 22 nm. However, one needs to recall that the XRD technique overestimates the crystallite size in that already small concentrations of large crystallites may dominate the intensities of XRD scans, while diffraction from small crystallites contribute mainly to the background intensity. Therefore, a microscopic technique, such as TEM is needed to countercheck for the size of supported particles (cf. Figure 3).

In Figure 3, we can recognize that the dispersion of the supported mixed ruthenium-iridium particles varies with composition. For the case of Ir_100@TiO_2, clearly many supported particles are discernible with a narrow size distribution. Quite in contrast, pure Ru_100@TiO_2 does not show any sign of supported particles. Instead, most of RuO_2 forms unsupported particles as shown with element mapping (cf. Figure S5). In between these extremes supported particles are clearly visible, but it is also obvious that its concentration decreases with increasing ruthenium content. In Table 2 we summarize the average particle sizes derived from TEM images in Figure 3. The particles size from TEM is systematically smaller than the XRD-derived ones that is explainable since XRD intensities are dominated by the bigger particles.

High resolution STEM together with element mapping supports this view. For pure Ir_100@TiO_2 there is no indication that unsupported IrO_2 particles are formed, while already for the Ru_25@TiO_2 agglomeration of mixed ruthenium-iridium particles is apparent (cf. Figure 4), although most of the particles adhere to the rutile TiO_2 support particles. Element mapping in Figure 4 reveals that all supported particles comprise a mixture of ruthenium and iridium; with 30 ± 10 mol% ruthenium that is reconciled with the nominal concentration of 25 mol% ruthenium. A separation into pure RuO_2 and IrO_2 can be ruled out since XRD reveals an average crystallite size of 8 nm (Table 2) for the active component in Ru_25@TiO_2 and such big particles of pure RuO_2 and IrO_2 conflicts with the identical intensity distribution of ruthenium and iridium in the EDS mappings in Figure 4.

The morphology of the pure Ru_100@TiO_2 sample is studied by HRTEM providing evidence that RuO_2 forms a thin layer (1–2 nm thick) of RuO_2 on rutile TiO_2 (Figure S6), while most of the RuO_2 agglomerates, forming larger particles that do not adhere to the TiO_2 support (cf. Figure S5). These larger RuO_2 agglomerates are responsible for the sharp (101) reflection in XRD (cf.

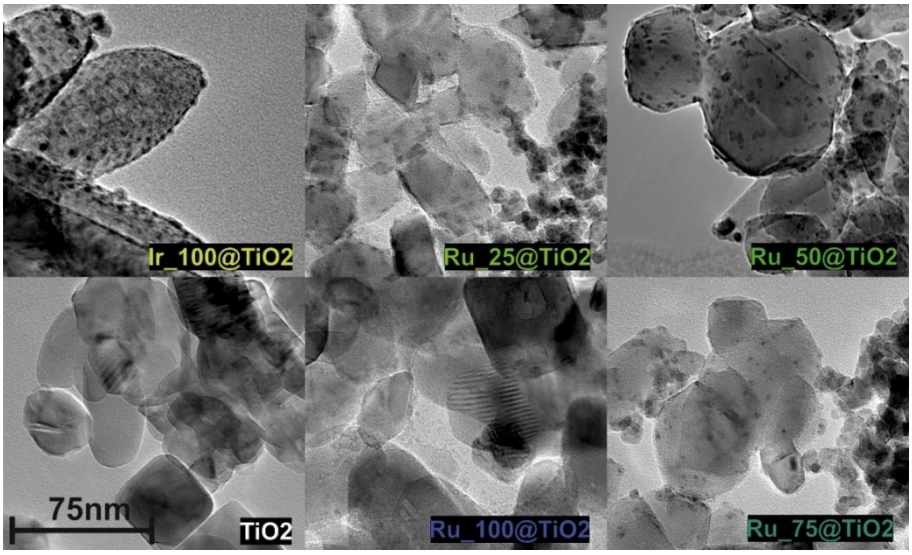


Figure 3. TEM images of as prepared Ru_*x*@TiO_2 samples at a magnification of 110,000 revealing high dispersion with a narrow size distribution for pure Ir_100@TiO_2. In the pure Ru_100@TiO_2 sample hardly any supported material can be discerned. The mixed supported oxides show a high dispersion of the active component on the support surface with a trend of increasing dispersion with higher amount of iridium. Overview TEM micrographs of lower magnification are presented in the supporting information (Figure S4).

© 2021 The Authors. ChemCatChem published by Wiley-VCH GmbH

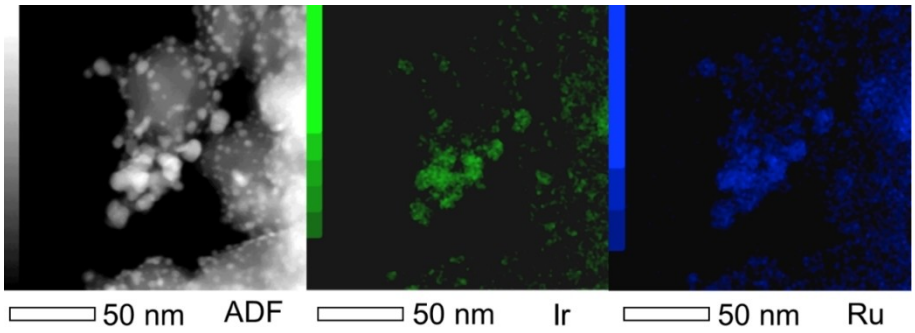


Figure 4. Annular dark field image and EDS-elemental mapping of the Ru_25@TiO_2 sample, indicating that the small particle on the surface of TiO_2 support consist of a mixture of ruthenium and iridium with 30 ± 10 mol% Ru, roughly in agreement with the nominal composition (25 mol% ruthenium).

Figure 2a) that corresponds to an averaged single crystalline particle size in the agglomerate of 22 nm (cf. Table 2).

For the comparison of activity data among various supported Ru_x@TiO_2 samples it is required that the space time yield *STY* is normalized to the active surface area. For mixed ruthenium-iridium powder samples[21] this can be accomplished by measuring the *BET surface area*. However, for supported catalysts this approach is not reasonable since the catalytically inactive support dominates the *BET surface area*. Therefore, we measured the relative active surface area by CO uptake experiments, assuming that the number of adsorbed CO molecules is strictly correlated with the *number of active sites* of the active component and independent of the actual composition of the mixed oxide catalyst. In Table 3 we summarize these experimental results.

As suggested by HRTEM and XRD, the active surface areas of Ir_100@TiO_2 and Ru_25@TiO_2 are the highest, while the ones of Ru_50@TiO_2 and Ru_75@TiO_2 are the lowest. Quite surprisingly, the active surface area of Ru_100@TiO_2 is high and apparently conflicts with the large average RuO_2 particle size of 22 nm as derived from XRD. However, HRTEM reveals that the TiO_2 particles are partly covered by a thin RuO_2 layer of 1–2 nm thickness. These layers are likely to be responsible for the observed high active surface area, but do not contribute to the XRD pattern.

Table 3. Number of active sites of supported Ru_x@TiO_2 derived by CO-pulse experiments normalized to the catalyst's mass and to the amount of active component given in mol. In addition, the BET surface areas are provided.

sample	# *active sites*/m_{cat} [μmol·g^{-1}]	# *active sites*/$n_{a.c.}$ [mmol·mol^{-1}]	*BET surface area* [$m^2 \cdot g^{-1}$]
Ir_100@TiO_2	103 ± 1	164	19
Ru_25@TiO_2	82 ± 1	130	12
Ru_50@TiO_2	54 ± 4	86	23
Ru_75@TiO_2	60 ± 3	96	17
Ru_100@TiO_2	82 ± 6	131	17

2.2. Kinetic data of methane combustion over mixed ruthenium-iridium supported on rutile-TiO_2

Figure 5 summarizes the light-off curves of methane combustion over supported catalysts Ru_*x*@TiO_2 with varying composition *x*; in Figure 5a the original experimental data are shown, while in Figure 5b these light-off curves are normalized to the *number of active sites* from Table 3. In the light-off experiments the temperature is linearly ramped with 1 °C·min^{-1} up to *T10* where the conversion *X* of the methane combustion reaction reaches 10% with a reaction feed of 2 sccm methane and 8 sccm O_2 balanced by 90 sccm N_2; generally, the temperature sweep rate needs to be low enough to maintain steady state conditions during the temperature ramp.

These light-off temperatures *T10* as well as *T2* (*X* = 2%) and *T5* (*X* = 5%) values are collected in Table 4. Ru_100@TiO_2 with RuO_2 as the active component clearly reveals the lowest activity in methane combustion. However, it is equally evident that not the pure Ir_100@TiO_2 (with IrO_2 as the active component) but instead Ru_25@TiO_2 is the most active catalyst in methane combustion for conversions lower than 10%. When normalizing

Table 4. Light-off temperatures *T2* (*X* = 2%), *T5* (*X* = 5%) and *T10* (*X* = 10%) for supported mixed Ru_*x*@TiO_2 materials applied to methane combustion reaction. Kinetic parameters: Apparent activation energies E_{act} and pre-factors STY_0 (normalized to the *mass of the catalysts)* $STYn_0$ (normalized to the *number of active sites*) as well as the reaction orders *R.O.* in oxygen and methane.

sample	*T2* [°C]	*T5* [°C]	*T10* [°C]	E_{act} [kJ mol^{-1}]	STY_0 [mol(CO_2)$h^{-1}kg_{cat}^{-1}$]	$STYn_0$ [mol(CO_2)·h^{-1}·(μmol a.s.)$^{-1}$]	*R.O.* in O_2	*R.O.* in CH_4
Ir_100@TiO_2	281	304	322	105	3×10^{10}	3×10^{5}	0.0	1.0
Ru_25@TiO_2	274	296	313	107	6×10^{10}	8×10^{5}	0.0	0.9
Ru_50@TiO_2	299	324	344	104	1×10^{10}	2×10^{5}	0.0	0.8
Ru_75@TiO_2	296	323	346	93	1×10^{9}	2×10^{4}	0.0	0.9
Ru_100@TiO_2	339	374	403	82	4×10^{7}	5×10^{2}	0.0	0.9

© 2021 The Authors. ChemCatChem published by Wiley-VCH GmbH

18673899, 2021, 18, Downloaded from https://chemistry-europe.onlinelibrary.wiley.com/doi/10.1002/cctc.202100858 by Cochrane Germany, Wiley Online Library on [28/11/2022]. See the Terms and Conditions (https://onlinelibrary.wiley.com/terms-and-conditions) on Wiley Online Library for rules of use; OA articles are governed by the applicable Creative Commons License

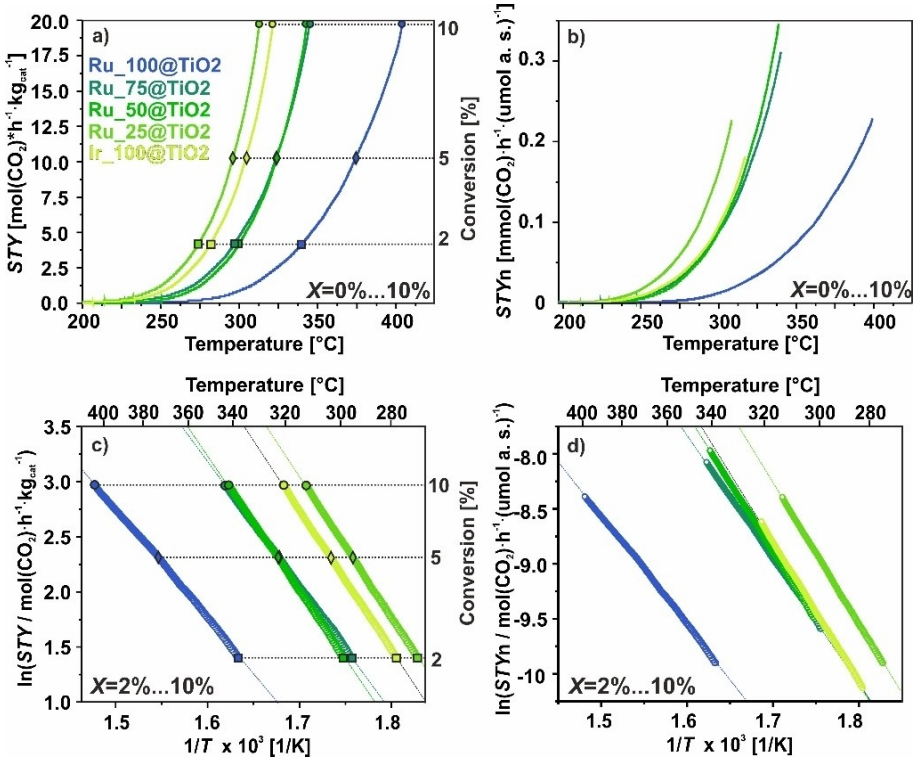


Figure 5. Light-off experiments for the catalytic CH_4 combustion reaction over supported mixed $Ru_xIr_{1-x}O_2$@TiO_2 samples normalized to the *mass of the catalyst* (a) and to the *number of active sites* (b). In all *STY* curves the conversion ranges from 0% to 10%, the total flow rate was 100 sccm with *Vol*%(CH_4): *Vol*%(O_2) = 2:8. Corresponding Arrhenius plots are shown in (c) for *STY* and (d) for STY_n normalized *to the number of active sites*.

the activity data to the *number of active sites* (cf. Figure 5b), Ir_100@TiO_2, Ru_50@TiO_2, and Ru_75@TiO_2 show similar activity that is substantially higher than pure Ru_100@TiO_2, but still significantly lower than that of Ru_25@TiO_2.

The activity data shown in Figure 5a,b can also be represented as Arrhenius plots (cf. Figure 5c,d) in order to extract kinetic data such as the apparent activation energies E_{act} and the pre-factors STY_0 which are compiled in Table 4. The apparent activation energies are independent of the normalization procedure, but the pre-factor values STY_0, $STYn_0$ depend of course on the normalization [Eqs. (4) and (5)] and are separately listed in Table 4.

$$STY = STY_0 \cdot \exp\left(-\frac{E_{act}}{RT}\right) \quad (4)$$

$$STYn = STYn_0 \cdot \exp\left(-\frac{E_{act}}{RT}\right) \quad (5)$$

The highest activity is paralleled by the highest values of the pre-factors, while the apparent activation energies counteract these values by high apparent activation energies for active catalysts and lower values for the less active catalyst. The pre-factor for Ru_100@TiO_2 is three order of magnitude lower than that of Ru_25@TiO_2, making Ru_100@TiO_2 substantially less active than Ru_25@TiO_2. A similar pattern in the apparent activation energies and pre-factors was encountered for the CO oxidation over mixed ruthenium-iridium oxide catalysts.[21]

To conclude the kinetic study, we performed experiments to determine the reaction order *R.O.* (cf. Figure 6). Here the ln(*STY*) is shown as a function of the logarithm of the reaction feed. The reaction temperature is chosen for each sample in a way that the conversion is $X = 10\%$ for a reaction mixture of 8 sccm O_2 and 2 sccm methane. After reaching *T10* the reaction order is determined by changing the volumetric concentration of oxygen from 8 sccm to 2 sccm in steps of 2 sccm while keeping the methane concentration constant at 2 sccm. Subsequently, the oxygen concentration is kept constant at 2 sccm and the methane concentration is decreased in steps of 0.5 sccm from 2 sccm to 1 sccm. The oxygen concentration is then increased in steps of 2 sccm back from 2 sccm to 8 sccm while the methane concentration is fixed at 1 sccm. Finally, the methane concentration is raised from 1 sccm to 1.5 sccm to 2 sccm, thereby returning to the starting gas composition. This protocol enables an investigation of the reaction order of oxygen and methane over a wide range of reaction conditions from oxidizing (*Vol*%(O_2) = 8%, *Vol*%(CH_4) = 2%), stoichiometric (*Vol*%(O_2) = 4%, *Vol*%(CH_4) = 2%) to reducing (*Vol*%(O_2) = 2%, *Vol*%(CH_4) = 2%) conditions. The reaction orders are summarized in Table 4. It turns out that the reaction order in O_2 in all cases is zero, while the reaction order in methane is close to unity. From these values we infer that the oxygen supply on the catalyst's surface is not rate limiting, while methane activation

© 2021 The Authors. ChemCatChem published by Wiley-VCH GmbH

18673899, 2021, 18, Downloaded from https://chemistry-europe.onlinelibrary.wiley.com/doi/10.1002/cctc.202100858 by Cochrane Germany, Wiley Online Library on [28/11/2022]. See the Terms and Conditions (https://onlinelibrary.wiley.com/terms-and-conditions) on Wiley Online Library for rules of use; OA articles are governed by the applicable Creative Commons License

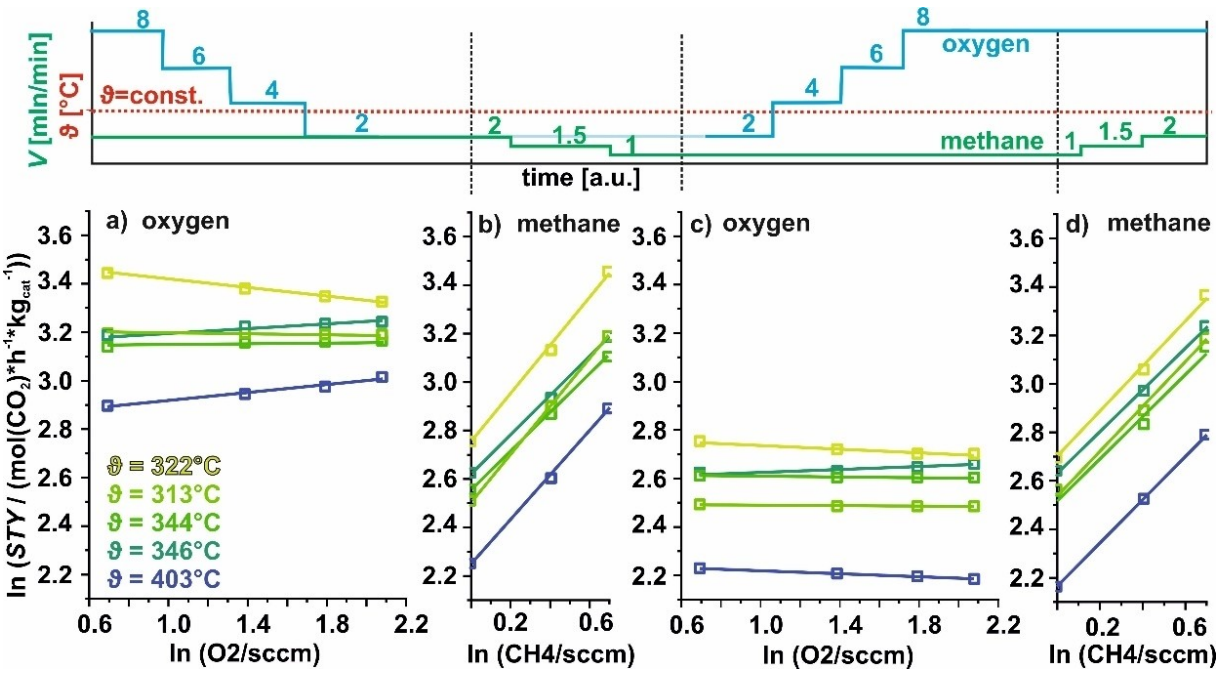


Figure 6. Reaction order for oxygen and methane in the methane combustion reaction over supported mixed $Ru_xIr_{1-x}O_2@TiO_2$ oxide samples with total flow rate of 100 sccm at a reaction temperature where the conversion is 10% (for 2 sccm methane and 8 sccm O_2 balanced by 90 sccm N_2). The methane concentration was constant and 2 sccm (a) and 1 sccm (c), while the oxygen concentration varies between 2 sccm to 8 sccm in steps of 2 sccm. To obtain the reaction in methane the oxygen concentration was kept fixed at 2 sccm (b) and 8 sccm (d) and the methane concentration was varied between 1 sccm to 2 sccm in steps of 0.5 sccm.

seems to dominate the reaction kinetics. Together with the apparent activation energies E_{act} these kinetic data culminates in the formal kinetic law [Eq. (6)]:

$$r = STY_0 \cdot \exp(-\frac{E_{act}}{RT}) \cdot [CH_4] \quad (6)$$

with the methane concentration $[CH_4]$. This kinetic law is consistent with that found for methane reaction on Ni-based catalysts.[31]

For comparison reason we carried out similar kinetics experiments for unsupported mixed ruthenium-iridium oxide powder catalysts with the same composition *x* as studied here and already characterized in a previous work.[21] These results are summarized in the supporting information (cf. Figure S7 and S8, Table S5), and similar conclusions can be drawn about activity and kinetics as for the supported catalyst. Pure RuO_2 turns out to be the least active catalyst in the methane combustion, while the Ru_25 sample is the most active catalyst. Also, the apparent activation energies and the reaction orders vary similarly as the corresponding supported samples„ indicating that the rutile-TiO_2 support does not significantly affect the intrinsic catalytic activity by additional metal-support interactions.

In Figure S9 light off experiments for both the unsupported and supported material are depicted. While for low conversion up to 10% mainly the intrinsic activity (microkinetics) is reflected, the performance of the catalysts at higher conversion is increasingly more governed by heat and mass transfer. From the complete light-off curves *T50*, *T70* and *T90* values (temperature for 50%, 70% and 90% conversion) can be extracted for the various catalyst's compositions. Up to the conversion *T10* the light off curves shown in Figure S9 correspond to the previous kinetic light off experiments of both unsupported (Figure S7) and supported (Figure 5) materials. For the unsupported material, the light off curves at higher conversions are in line with the extrapolation based on corresponding activation energies from Table S5. Transport limitations seem to occur quite late allowing Ru_25, Ru_75 and Ir_100 to reach 90% conversion at temperatures lower than 475 °C. In the case of the supported materials the trend of the light-off curves changes. Table 5 summarizes the light off temperatures *T50*, *T70* and *T90* for both unsupported and supported materials.

The lowest *T90* value is revealed for the unsupported Ru_25 catalyst that underlines its high catalytic activity throughout the

Table 5. Light-off temperatures *T50, T70 and T90* for both unsupported mixed Ru_*x* and supported mixed Ru_*x*@TiO_2 samples applied to the methane combustion reaction. The reproducibility of the light-off temperatures is ±5 °C.

sample	*T50* [°C]	*T70* [°C]	*T90* [°C]	sample	loading [mol%]/ [wt%]	*T50* [°C]	*T70* [°C]	*T90* [°C]
Ir_100	*400*	*422*	*465*	Ir_100@TiO_2	5/11	*346*	*359*	*447*
Ru_25	*360*	*371*	*408*	Ru_25@TiO_2	5/10	*364*	*420*	-
Ru_50	*416*	*458*	-	Ru_50@TiO_2	5/9	*421*	*473*	-
Ru_75	*388*	*405*	*447*	Ru_75@TiO_2	5/7	*363*	*385*	*469*
Ru_100	–	–	–	Ru_100@TiO_2	5/6	–	–	–

© 2021 The Authors. ChemCatChem published by Wiley-VCH GmbH

18673899, 2021, 18, Downloaded from https://chemistry-europe.onlinelibrary.wiley.com/doi/10.1002/cctc.202100858 by Cochrane Germany, Wiley Online Library on [28/11/2022]. See the Terms and Conditions (https://onlinelibrary.wiley.com/terms-and-conditions) on Wiley Online Library for rules of use; OA articles are governed by the applicable Creative Commons License

whole conversion range, while Ru_75 is the second best performing catalyst. For the supported materials, the catalytic performance of Ru_25@TiO_2 above a conversion of 10% becomes inferior compared to the pure Ir_100@TiO_2 but also to the Ru_75@TiO_2 sample. Altogether, $Ru_{0.75}Ir_{0.25}O_2$ reveals a surprisingly good catalytic performance for both supported and unsupported materials.

After the catalytic and kinetic experiments, the Ru_*x*@TiO_2 catalysts were post-characterized by TEM (cf. Figure S10). A comparison with the as-prepared Ru_*x*@TiO_2 catalysts reveals that no reaction-induced alterations are discernible, i.e., the catalysts are stable under the applied reaction conditions.

3. Discussion

3.1. Synthesis

We successfully synthesized mixed $Ru_xIr_{1-x}O_2$ oxide supported on rutile-TiO_2 with well-defined composition *x*. In all cases 5 mol% of active component was employed, in order to allow for in-depth characterization of the active component by XRD, XPS, TEM, and CO uptake experiments. Most notably, XPS and also STEM element mapping indicate that the composition *x* of mixed $Ru_xIr_{1-x}O_2$ corresponds to that of the molar ratio of iridium and ruthenium precursors employed in the synthesis, clearly demonstrating our high level of control on the composition *x*. We should emphasize that a similar level of control of the composition *x* of mixed $Ru_xIr_{1-x}O_2$ cannot be achieved by simple impregnation methods.

Rutile-TiO_2 particles serve here as nucleation centers in the Pechini method. While the dispersion of pure IrO_2 particles turns out to be high, deposition of pure RuO_2 on rutile TiO_2 is less clear-cut. According to HRTEM, RuO_2 forms thin layers on rutile-TiO_2 and in addition unsupported larger RuO_2 particles. This observation is consistent with a previous study, where pure RuO_2 was reported to grow epitaxially on rutile-TiO_2 but not on anatase TiO_2 particles.[32] TEM clearly reveals that the other Ru_*x*@TiO_2 samples with ruthenium compositions of 25 mol%, 50 mol%, and 75 mol% form supported particles besides agglomerates of unsupported mixed ruthenium-iridium oxide particles with the density of supported particles being significantly lower than that of Ir_100@TiO_2.

Obviously, pure IrO_2 and pure RuO_2 adhere differently to the supporting rutile-TiO_2 particles. Surface science studies revealed rutile RuO_2 to form a strained pseudomorphic RuO_2(110) layer adopting the surface lattice constants of the supporting rutile-TiO_2(110),[24] while rutile IrO_2(110) grows with much less strain on rutile-TiO_2(110).[25,33] Since the surface energy of IrO_2 is substantially higher than that of TiO_2 and the interfacial energy IrO_2/TiO_2 remains high, this may explain why IrO_2 forms particles rather than a wetting film on rutile TiO_2 with a small surface and interface area. Due to the quasi pseudomorphic growth of RuO_2 on rutile-TiO_2, the interfacial energy RuO_2/TiO_2 is low so that RuO_2 is now able to wet partly the TiO_2 particles, despite similar surface energies of RuO_2 and IrO_2.[34] Further growth of RuO_2 proceeds in separate particles with its native lattice constants. Obviously, this is energetically more favorable than increasing the RuO_2 film thickness beyond 1–2 nm.

CO uptake experiments successfully quantify the *number of active sites* or the relative active surface area for Ru_*x*@TiO_2 (cf. Table 3). The *number of active sites* is found to be high for Ir_100@TiO_2, while with increasing concentration of ruthenium the *number of active sites* decreases by a factor of 2–3. This decline in active sites can be related to the decreased concentration of supported particles. However, for pure Ru_100@TiO_2 the *number of active sites* (cf. Table 3) is surprisingly high and not reconciled with large RuO_2 particles evidenced by XRD. The high active surface area of Ru_100@TiO_2 is attributed to the observed thin layer growth of RuO_2 on rutile-TiO_2.

3.2. Methane combustion activity

We studied the activity and the kinetics of catalytic methane combustion over supported Ru_*x*@TiO_2 and unsupported powder Ru_*x* catalysts with varying compositions *x* ranging from pure RuO_2 to pure IrO_2 in steps of 25 mol%. To the best of our knowledge, these are the first catalytic methane combustion studies of this mixed oxide system. A comparison between supported and unsupported catalysts reveals practically identical trends in the activity for $X=0\%$ to $X=10\%$ and identical kinetics as a function of the composition. Therefore, the rutile TiO_2 support seems to have virtually no impact on the microkinetics of the methane combustion. However, for higher conversions the different dispersions of the active component on the support material seems to differently influence the heat and mass transfer which lead to re-ordering of the light-off curves. We have to bear in mind that this situation may change when the TiO_2 support is replaced for instance by CeO_2 or Al_2O_3, where charge transfer and spill-over phenomena are known to be operative.[35] At least for Pd-based catalysts, the standard catalyst for methane combustion,[3] the support has shown to play an important role.[1,36] For Pd embedded in CeO_2 the activity in methane combustion could be increased considerably.[37] Recall that under typical reaction conditions of methane combustion not metallic Pd but rather PdO is the active phase.[38]

In our low conversion catalytic tests (cf. Figure 5) the most active catalyst turned out to be Ru_25@TiO_2 (Ru_25) followed by Ir_100@TiO_2 (Ir_100) and then with increasing ruthenium concentration the activity declines steadily with pure Ru_100@TiO_2 (Ru_100) being by far the least active catalyst. Pure IrO_2 is substantially more efficient than pure RuO_2 in methane combustion. This finding is in accordance with surface science experiments which demonstrated that methane can be activated even at low temperature on IrO_2(110),[20] while under the very same conditions RuO_2(110) is virtually inactive.[39] Obviously, methane activation is an important step in methane combustion and therefore Ru_100@TiO_2 is the least active catalyst among the homologous series Ru_*x*@TiO_2. From these surface science studies it is quite surprising that pure RuO_2 is active at all in methane combustion. But the observed activity of RuO_2 is consistent with a recent study where RuO_2 supported

© 2021 The Authors. ChemCatChem published by Wiley-VCH GmbH

18673899, 2021, 18, Downloaded from https://chemistry-europe.onlinelibrary.wiley.com/doi/10.1002/cctc.202100858 by Cochrane Germany, Wiley Online Library on [28/11/2022]. See the Terms and Conditions (https://onlinelibrary.wiley.com/terms-and-conditions) on Wiley Online Library for rules of use; OA articles are governed by the applicable Creative Commons License

on Gamma Alumina was discussed as alternative catalyst for methane combustion.[40]

Pure RuO_2(110) is, however, known to be an excellent catalyst in the CO oxidation reaction,[22] while on IrO_2(110) the adsorption of CO was found to be much stronger than on RuO_2.[41] In fact, RuO_2 has shown to be more active in the CO oxidation than IrO_2.[21] Therefore, we expected a synergism effect of ruthenium on the activity of methane combustion. Indeed, 25 mol% ruthenium (75 mol% iridium) in the mixed oxide catalysts reveals a significant improvement of the catalytic performance in methane combustion. In order to decide whether this improvement is due to the higher dispersion of $Ru_xIr_{1-x}O_2$ on rutile TiO_2 or to an increase in intrinsic activity, we needed to normalize the *STY* values to the *number of active surface sites* as provided by CO uptake experiments (Table 3). Since the trend in activity among Ru_*x*@TiO_2 is not affected by this normalization procedure, we ascribe the improved performance of the Ru_25@TiO_2 sample in methane combustion to an increase in the intrinsic activity of the mixed oxide. A very similar trend in activity is found for the unsupported Ru_*x* catalyst (supporting information) when normalizing *STY* to the *BET surface area.*

The superior performance of Ru_25@TiO_2 in methane combustion points towards an intimate interplay of methane activation (by IrO_2) and the subsequent formation of an oxygenated reaction intermediate from the methyl fragment, such as CO, CH_2O, or CHO_2 or the final oxidation step to CO_2 by RuO_2. Of course, RuO_2 may equally promote the oxidation of the abstracted H from methane to form water. This may be evident when again considering corresponding surface science experiments: Hydrogen adsorption and subsequent annealing of the sample leads to water formation between 127 °C to 227 °C for RuO_2(110),[42] but results in a broad water desorption feature ranging from 127 °C to 477 °C for IrO_2(110).[43]

Also quite surprising is the observation that Ru_75@TiO_2 and Ru_75, although being not the most active catalyst, are substantially more active than Ru_100@TiO_2 and Ru_100 (Figure 5d) by decreasing the reaction temperature *T10* by 80 °C. This means that already a relatively small concentration of iridium improves the low temperature methane activity of RuO_2 considerably.

The observed kinetics (for conversions lower than 10%) of the methane combustion over unsupported Ru_*x* (Table S3) and supported Ru_*x*@TiO_2 (cf. Table 4) are virtually identical, corroborating the view that the rutile-TiO_2 support does hardly affect the catalytic behavior of the active component. From the kinetic data of Ru_*x*@TiO_2 in Table 4, the catalysts can be grouped in two categories, one with a high concentration of ruthenium (50 mol%, 75 mol%) and the other with low ruthenium concentration (0 mol%, 25 mol%, 50 mol%). The apparent activation energies and the pre-factors of the ruthenium-rich catalysts (80–90 $kJ \cdot mol^{-1}$) are significantly lower than those of the iridium-rich catalysts (105 ± 2 $kJ \cdot mol^{-1}$). The most active catalyst Ru_25@TiO_2 reveals the highest apparent activation energy and the highest pre-factor, resulting in a catalyst that at higher reaction temperature is even more active than the others. Obviously, the higher apparent activation energy is overcompensated by the high value of the pre-factor. This compensation effect is known as the Cremer-Constable relation. Similar apparent activation energies as for the present iridium-rich catalysts were also reported for supported Pd and Pt based catalysts.[3]

For methane combustion over both Ru_*x*@TiO_2 and Ru_*x*, the reaction order in methane is close to one, while that in oxygen is zero. Similar reaction orders in methane and oxygen are reported for Pd-based catalyst.[3] These reaction orders for the total methane oxidation reaction over Ru_*x*@TiO_2 and Ru_*x* agree remarkably well with those reported for other noble metal catalysts.[44]

For the unsupported material Ru_25 and Ru_75 remain the most active catalysts in the entire temperature and conversion range. Due most likely to transport limitations which vary among the supported materials with their varying dispersions and particle sizes, the catalytic activity of Ru_25@TiO_2 decreases with increasing conversion and Ir100@TiO_2 and Ru_75@TiO_2 become the most promising catalysts. At high conversions, the catalytic performance of Ru_75 and Ru_75@TiO_2 approaches even that of pure Ir100 and Ir100@TiO_2 catalysts.

In Table 6 the catalytic performance (*T50* and *T90*) of Ir100@TiO_2 and Ru_75@TiO_2 in the catalytic methane combustion is compared to supported Pd catalysts, defining the benchmark catalyst for low temperature methane combustion. Unfortunately, a direct comparison of *T50* and *T90* values is hampered by differences in the mass of catalyst, the loading of the active component, the gas composition fed to the reactor, and the contact time with the catalyst material; all these factors affect the light-off curves.

From the *T50* and *T90* values summarized in Table 6 we conclude that the activities of both Ir_100@TiO_2 and Ru_75@TiO_2 are comparable to that of Pd@Al_2O_3. A direct comparison of the Ir_100@TiO_2 and Ru_75@TiO_2 with Pd@TiO_2 reveals that *T90* is 44 to 66 °C lower. However, it needs to be noted that in our study the methane fed is two times higher and the amount of the active component is about 2 to 3 times lower than in the study of Pd@TiO_2. Besides activity, a critical issue in catalytic methane combustion is catalyst poisoning by water, sulfur and other constituents in the exhaust gas[51] that needs to be studied for mixed ruthenium/iridium oxide

Table 6. Comparison of *T50* and *T90* values of Ir_100@TiO_2 and Ru_75@TiO_2 with those of Pd@Al_2O_3 and Pd@TiO_2 under similar reaction conditions.

sample	mass of catalyst [mg]	loading	flow rate [sccm]	%CH_4	*T50* [°C]	*T90* [°C]
Ir_100@TiO_2	20	5 mol% (10 wt%)	100	2	346	447
Ru_75@TiO_2	20	5 mol% (7 wt%)	100	2	363	469
Pd@TiO_2[45]	100	5 wt%	100	0.8	331	403
Pd@Al_2O_3[46]	120	5 wt%	100	1	≈350	≈400
Pd@Al_2O_3[47]	100	0.5 wt%	100	1	≈395	≈460
Pd@Al_2O_3[48]	200	2 wt%	100	0.2	≈600	≈660
Pd@Al_2O_3[49]	≈20	5 wt%	200	0.25	340	560
Pd@Al_2O_3[50]	320	2 wt%	100	1	460	–

© 2021 The Authors. ChemCatChem published by Wiley-VCH GmbH

18673899, 2021, 18, Downloaded from https://chemistry-europe.onlinelibrary.wiley.com/doi/10.1002/cctc.202100858 by Cochrane Germany, Wiley Online Library on [28/11/2022]. See the Terms and Conditions (https://onlinelibrary.wiley.com/terms-and-conditions) on Wiley Online Library for rules of use; OA articles are governed by the applicable Creative Commons License

catalysts in the future. We do not expect that IrO_2 catalysts will replace Pd-based catalysts for the methane combustion due to the limited amount of mined Ir (6 t/a). On the other hand, RuO_2 is not an efficient oxidation catalyst for methane combustion, and under oxidizing conditions, RuO_2 is vulnerable to over-oxidation to form volatile RuO_3 and RuO_4 above 500–600 °C.[52] However, mixing 25 mol% or less of IrO_2 into RuO_2 improves the activity steeply and thermally stabilizes RuO_2. Since Ru is significantly more abundant than Ir (30 t/a) and about eight times less expensive than Pd, RuO_2 with little IrO_2 could therefore be a promising option for catalytic methane combustion.

3.3. Molecular insight

From kinetic data only, we cannot decipher the actual reaction mechanism of methane combustion over $Ru_xIr_{1-x}O_2$. Instead, we would need to perform operando spectroscopy experiments to identify the reaction intermediates and to conduct first principles kinetics simulations to simulate the experimental kinetics. However, from experimental kinetic data we can draw some mechanistic conclusions about the catalytic reaction. For instance, from a reaction order in methane of one and a reaction order in oxygen of zero we can safely conclude that methane activation constitutes the rate limiting step in the combustion process. A similar conclusion was previously drawn for supported Ir-clusters.[53] A reaction order in oxygen of zero means that always enough surface oxygen is available at the active sites, thus favoring a Mars-van-Krevelen mechanism over the Langmuir-Hinshelwood mechanism. For a firm conclusion about the question of Langmuir-Hinshelwood versus Mars-van Krevelen mechanism one needs to conduct isotope labelling experiments of ^{16}O and ^{18}O[31,54] which are, however, beyond the scope of the present paper.

First principle calculations for methane combustion over $Ru_xIr_{1-x}O_2$ are not available. However, for a similar catalyst system PdO(101), a recent first principle microkinetic study[38] has shown that the reaction mechanism constitute a combination of Langmuir Hinshelwood and Mars van Krevelen mechanism depending on the reaction temperature.

In the methane activation step two different surface sites are involved. Vacant undercoordinated metal sites (likely Ir sites) are required to adsorb the methyl group, while undercoordinated surface oxygen sites can accommodate the abstracted hydrogen species. Therefore, these surface species participate in the catalytically active sites, i.e., the number of active sites is proportional to the number of surface metal sites.

There are DFT studies available for the methane activation on IrO_2(110).[16,18] From these calculations the apparent activation energy for methane activation turns out to be negative since the adsorption energy of intact methane is with 60 $kJ \cdot mol^{-1}$ higher than the actual activation barrier for dissociation (about 30 $kJ \cdot mol^{-1}$). This result is not reconciled with the observed apparent activation energies of 80–110 $kJ \cdot mol^{-1}$ depending on the composition of the mixed Ru–Ir oxide. However, this variation in apparent energy fits remarkably well to the adsorption energy of oxygen on IrO_2 and RuO_2. From thermal desorption spectroscopy[41,55] of IrO_2(110) and RuO_2(110) the O–Ir bond is shown to be slightly stronger than the Ru–O bond.[56] Under lean methane oxidation reaction conditions the catalyst's surface is likely saturated and therefore blocked by adsorbed oxygen so that methane activation is suppressed. The apparent activation energy may therefore correspond to the activation of oxygen desorption, thereby liberating metallic adsorption sites for methane activation.

4. Conclusions

We present here stable activity data of methane combustion on mixed ruthenium-iridium based catalysts Ru_*x*@TiO_2 supported on rutile-TiO_2 in comparison with those on unsupported Ru_*x* catalysts. Both types of mixed catalysts are prepared by a (modified) Pechini synthesis in order to ensure full control of the composition *x in* the mixed $Ru_xIr_{1-x}O_2$. From the direct comparison of supported and unsupported catalysts, it turns out that the rutile-TiO_2 support does not affect the catalytic performance in methane combustion.

Pure Ir_100@TiO_2 is much more active in the combustion of methane than pure Ru_100@TiO_2, with the former exhibiting an onset temperature of about 220 °C that is similar to onset temperatures encountered for Pd and Pt based catalysts.[3,44] The most active catalyst among the series of Ru_*x*@TiO_2 and Ru_*x* turned out to be Ru_25@TiO_2 (Ru_25) with an apparent activation energy of 105 $kJ \cdot mol^{-1}$ and a required reaction temperature of 313 °C to achieve 10% conversion at *GHSV* of 164.000 h^{-1} (corresponding to 345.000 $ml \cdot g^{-1} \cdot h^{-1}$ if normalized to *mass of catalyst*). The catalytic performance of IrO_2@TiO_2 and $Ru_{0.75}Ir_{0.25}O_2$@TiO_2 in methane combustion in terms of *T50* and *T90* (the reaction temperature to achieve 50% and 90% conversion) is comparable to that reported for typical Pd catalysts (cf. Table 6).

Ru_75@TiO_2 and Ru_75, although being not the most active catalyst, are substantially more active than Ru_100@TiO_2 and Ru_100 by decreasing the *T10* temperature by 80 °C; the onset temperature of Ru_75@TiO_2 is about 230 °C. This means that already a small concentration of iridium improves the activity of RuO_2 in methane combustion considerably.

From a reaction order of unity in methane we conclude that the methane activation step is rate determining in the methane combustion over mixed ruthenium-iridium based catalysts. There is evidence that the apparent activation energy is related to the activation energy of molecular oxygen desorption from the catalyst's surface. In this way active metal sites are liberated to accommodate the methyl group in methane activation step. Methane activation by IrO_2, although mandatory, is however only part of the story. The further oxidation of methyl to CO_2 is apparently another important step which is promoted by the addition of RuO_2.

© 2021 The Authors. ChemCatChem published by Wiley-VCH GmbH

18673899, 2021, 18, Downloaded from https://chemistry-europe.onlinelibrary.wiley.com/doi/10.1002/cctc.202100858 by Cochrane Germany, Wiley Online Library on [28/11/2022]. See the Terms and Conditions (https://onlinelibrary.wiley.com/terms-and-conditions) on Wiley Online Library for rules of use; OA articles are governed by the applicable Creative Commons License

Appendix A. Supplementary data

Supplementary data associated with this article can be found in the online version.

Acknowledgements

We thank financial support by the DFG within the SPP2080. We acknowledge support from the Laboratory of Materials Research at the JLU. Sebastian Werner is acknowledged for performing the BET experiments. Felix Walther is acknowledged for taking the XP spectra. Goran Drazic acknowledges the financial support from Slovenian Research Agency (P2-0393). Open access funding enabled and organized by Projekt DEAL.

Conflict of Interest

The authors declare no conflict of interest.

Keywords: Methane combustion · heterogeneous catalysis · mixed $Ru_xIr_{1-x}O_2$ oxide catalysts · catalytic tests · kinetic experiments

[1] D. Ciuparu, M. R. Lyubovsky, E. Altman, L. D. Pfefferle, A. Datye, *Catal. Rev. Sci. Eng.* **2002**, *44*, 593–649.
[2] H. Hao, Z. Liu, F. Zhao, W. Li, *Renewable Sustainable Energy Rev.* **2016**, *62*, 521–533.
[3] L. He, Y. Fan, J. Bellettre, J. Yue, L. Luo, *Renewable Sustainable Energy Rev.* **2020**, *19*.
[4] S. Perathoner, G. Centi, *Science and Technology Roadmap on Catalysis for Europe*, EU commission, **2016**.
[5] J. Chen, H. Arandiyan, X. Gao, J. Li, *Catal. Surv. Asia* **2015**, *19*, 140–171.
[6] A. Raj, *Johnson Matthey Tech. Rev.* **2016**, *60*, 228–235.
[7] T. v Choudhary, S. Banerjee, V. R. Choudhary, *Appl. Catal. A* **2002**, *234*, 1–23.
[8] V. Bashan, Y. Ust, *Int. J. Energy Res.* **2019**, *43*, 7755–7789.
[9] J. Yang, Y. Guo, *Chin. Chem. Lett.* **2018**, *29*, 252–260.
[10] M. Monai, T. Montini, R. J. Gorte, P. Fornasiero, *Eur. J. Inorg. Chem.* **2018**, *2018*, 2884–2893.
[11] J. H. Lee, D. L. Trimm, *Fuel Process. Technol.* **1995**, *42*, 339–359.
[12] R. Burch, F. J. Urbano, *Appl. Catal. A* **1995**, *124*, 121–138.
[13] Q. Duan, C. Zhang, S. Sun, Y. Pan, X. Zhou, Y. Liu, K. Chen, C. Li, X. Wang, W. Li, *J. Mater. Chem. A* **2020**, *8*, 7395–7404.
[14] M. Lyubovsky, L. Pfefferle, *Appl. Catal. A* **1998**, *173*, 107–119.
[15] K. Murata, D. Kosuge, J. Ohyama, Y. Mahara, Y. Yamamoto, S. Arai, A. Satsuma, *ACS Catal.* **2020**, *10*, 1381–1387.
[16] Z. Liang, T. Li, M. Kim, A. Asthagiri, J. F. Weaver, *Science* **2017**, *356*, 299–303.
[17] M. Kim, A. D. Franklin, R. Martin, Y. Bian, J. F. Weaver, A. Asthagiri, *J. Catal.* **2020**, *383*, 181–192.
[18] C. C. Wang, S. S. Siao, J. C. Jiang, *J. Phys. Chem. C* **2012**, *116*, 6367–6370.
[19] Y. C. Liu, C. H. Yeh, Y. F. Lo, S. Nachimuthu, S. D. Lin, J. C. Jiang, *J. Catal.* **2020**, *385*, 265–273.
[20] W. Kumsung, M. Chareonpanich, P. Kongkachuichay, S. Senkan, A. Seubsai, *Catal. Commun.* **2018**, *110*, 83–87.
[21] O. Khalid, T. Weber, G. Drazic, I. Djerdj, H. Over, *J. Phys. Chem. C* **2020**, *124*, 18670–18683.
[22] S. Wendt, A. P. Seitsonen, Y. D. Kim, M. Knapp, H. Idriss, H. Over, *Surf. Sci.* **2002**, *505*, 137–152.
[23] M. P. Pechini, *US Patent 3,330,697* **1967**, *2*.
[24] Y. He, D. Langsdorf, L. Li, H. Over, *J. Phys. Chem. C* **2015**, *119*, 2692–2702.
[25] M. J. S. Abb, T. Weber, L. Glatthaar, H. Over, *Langmuir* **2019**, *35*, 7720–7726.
[26] X. Yang, Q. Gao, Z. Zhao, Y. Guo, Y. Guo, L. Wang, Y. Wang, W. Zhan, *Appl. Catal. B* **2018**, *239*, 373–382.
[27] J.-S. Moon, E.-G. Kim, Y.-K. Lee, *J. Catal.* **2014**, *311*, 144–152.
[28] Z. Hu, Z. Wang, Y. Guo, L. Wang, Y. Guo, J. Zhang, W. Zhan, *Environ. Sci. Technol.* **2018**, *52*, 9531–9541 (supporting information).
[29] R. Kötz, S. Stucki, *Electrochim. Acta* **1986**, *31*, 1311–1316.
[30] A. H. Reksten, A. E. Russel, P. W. Richardson, S. J. Thompson, K. Mathisen, F. Seland, S. Sunde, *Phys. Chem. Chem. Phys.* **2019**, *21*, 12217–12230.
[31] J. Wei, E. Iglesia, *J. Catal.* **2004**, *224*, 370–383.
[32] G. Xiang, X. Shi, Y. Wu, J. Zhuang, X. Wang, *Sci. Rep.* **2012**, *2*.
[33] T. Weber, V. Vonk, M. J. S. Abb, J. Evertsson, M. Sandroni, J. Drnec, A. Stierle, E. Lundgren, H. Over, *J. Phys. Chem. Lett.* **2020**, *2*, 9057–9062.
[34] G. Novell-Leruth, G. Carchini, N. López, *J. Chem. Phys.* **2013**, *138*, 194706.
[35] Y. Lykhach, J. Kubát, A. Neitzel, N. Tsud, M. Vorokhta, T. Skála, F. Dvořák, Y. Kosto, K. C. Prince, V. Matolín, V. Johánek, J. Mysliveček, J. Libuda, *J. Chem. Phys.* **2019**, *151*, 204703.
[36] J. Nilsson, P. A. Carlsson, S. Fouladvand, N. M. Martin, J. Gustafson, M. A. Newton, E. Lundgren, H. Grönbeck, M. Skoglundh, *ACS Catal.* **2015**, *5*, 2481–2489.
[37] M. Cargnello, J. J. Delgado Jaén, J. C. Hernández Garrido, K. Bakhmutsky, T. Montini, J. J. Calvino Gámez, R. J. Gorte, P. Fornasiero, *Science* **2012**, *337*, 713–717.
[38] M. van den Bossche, H. Grönbeck, *J. Am. Chem. Soc.* **2015**, *137*, 12035–12044.
[39] U. Erlekam, U. A. Paulus, Y. Wang, H. P. Bonzel, K. Jacobi, G. Ertl, *Zeitschrift für Phys. Chemie* **2005**, *219*, 891–903.
[40] T. Chomboon, W. Kumsung, M. Chareonpanich, S. Senkan, A. Seubsai, *Catalysts* **2019**, *9*, 335.
[41] M. J. S. Abb, T. Weber, D. Langsdorf, V. Koller, S. M. Gericke, S. Pfaff, M. Busch, J. Zetterberg, A. Preobrajenski, H. Grönbeck, E. Lundgren, H. Over, *J. Phys. Chem. C* **2020**, *124*, 15324–15336.
[42] M. Knapp, D. Crihan, A. P. Seitsonen, E. Lundgren, A. Resta, J. N. Andersen, H. Over, *J. Phys. Chem. C* **2007**, *111*, 5363–5373.
[43] T. Li, M. Kim, Z. Liang, A. Asthagiri, J. F. Weaver, *Top. Catal.* **2018**, *61*, 397–411.
[44] P. Gélin, L. Urfels, M. Primet, E. Tena, *Catal. Today* **2003**, *83*, 45–57.
[45] J. Okal, M. Zawadzki, K. Baranowska, *Appl. Catal. B* **2016**, *194*, 22–31.
[46] T. R. Baldwin, R. Burch, *Appl. Catal.* **1990**, *66*, 337–358.
[47] Y. Chen, J. Lin, X. Chen, S. Fan, Y. Zheng, *Catal. Sci. Technol.* **2021**, *11*, 152–161.
[48] P. Gélin, M. Primet, *Appl. Catal. B* **2002**, *39*, 1–37.
[49] H. Yoshida, T. Nakajima, Y. Yazawa, T. Hattori, *Appl. Catal. B* **2007**, *71*, 70–79.
[50] O. Demoulin, B. le Clef, M. Navez, P. Ruiz, *Appl. Catal. A* **2008**, *344*, 1–9.
[51] N. M. Kinnunen, J. T. Hirvi, K. Kallinen, T. Maunula, M. Keenan, M. Suvanto, *Appl. Catal. B* **2017**, *207*, 114–119.
[52] Z. Hölgye, M. Křivánek, *J. Radioanal. Chem.* **1978**, *42*, 133–141.
[53] J. W. Wei, E. Iglesia, *Angew. Chem. Int. Ed.* **2004**, *43*, 3685–3688; *Angew. Chem.* **2004**, *116*, 3771–3774.
[54] C. A. Müller, M. Maciejewski, R. A. Koeppel, R. Tschan, A. Baiker, *J. Phys. Chem.* **1996**, *100*, 20006–20014.
[55] R. Martin, M. Kim, M. S. Shariff, F. Feng, R. J. Meyer, A. Asthagiri, J. F. Weaver, *J. Chem. Phys.* **2020**, *152*, 074712.
[56] Y. D. Kim, A. P. Seitsonen, S. Wendt, C. Wang, C. Fan, K. Jacobi, H. Over, G. Ertl, *J. Phys. Chem. B* **2001**, *105*, 3752–3758.

Manuscript received: June 14, 2021
Revised manuscript received: July 8, 2021
Accepted manuscript online: July 12, 2021
Version of record online: August 12, 2021

© 2021 The Authors. ChemCatChem published by Wiley-VCH GmbH

18673899, 2021, 18, Downloaded from https://chemistry-europe.onlinelibrary.wiley.com/doi/10.1002/cctc.202100858 by Cochrane Germany, Wiley Online Library on [28/11/2022]. See the Terms and Conditions (https://onlinelibrary.wiley.com/terms-and-conditions) on Wiley Online Library for rules of use; OA articles are governed by the applicable Creative Commons License